

Effects of Particle Size and Polytype on the Redox Reversibility of the Layered $\text{Na}_{0.76}\text{Ni}_{0.38}\text{Mn}_{0.62}\text{O}_2$ Electrode

Eun Jeong Kim, Ryoichi Tatara, Tomooki Hosaka, Kei Kubota, Shinichi Kumakura, and Shinichi Komaba*



Cite This: *ACS Appl. Energy Mater.* 2024, 7, 1015–1026



Read Online

ACCESS |



Metrics & More



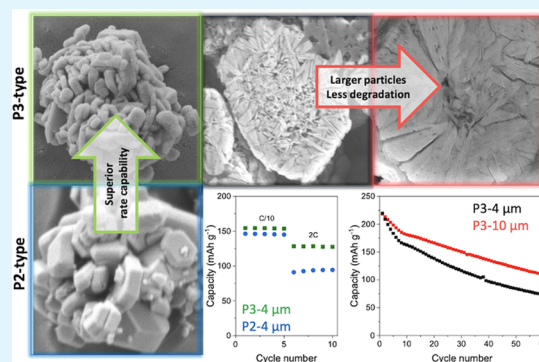
Article Recommendations



Supporting Information

ABSTRACT: Layered sodium nickel manganese oxides ($\text{Na}_x\text{Ni}_y\text{Mn}_{1-y}\text{O}_2$) have gained great interest as one of the positive electrode materials in sodium-ion batteries toward sustainable energy storage systems. However, the significant capacity fade of those materials necessities to be solved for practical application. Partial substitutions for Ni and Mn at the expense of delivered capacity have been widely suggested to address the poor cycle life, whereas relatively little investigation on particle morphology and/or surface engineering has been carried out. Herein, P3- and P2-type $\text{Na}_{0.76}\text{Ni}_{0.38}\text{Mn}_{0.62}\text{O}_2$ powders were prepared using 4 and 10 μm ($\text{Ni}_{0.38}\text{Mn}_{0.62}$)(OH)₂ precursors to understand the influence of primary and secondary particle sizes and polytype on their electrochemical performance in Na cells. P3-type $\text{Na}_{0.76}\text{Ni}_{0.38}\text{Mn}_{0.62}\text{O}_2$ with smaller primary particles and the absence of impurity have superior cyclability and rate capability compared to the P2-type one. In addition, larger secondary particles improve cycling performance in both polytypes. Formation of microcracks is inevitable over 100 cycles, especially with the upper cutoff voltage of 4.4 V; however, more severe pulverization and microcracks are shown in 4 μm P3-type $\text{Na}_{0.76}\text{Ni}_{0.38}\text{Mn}_{0.62}\text{O}_2$ compared to 10 μm P3-type $\text{Na}_{0.76}\text{Ni}_{0.38}\text{Mn}_{0.62}\text{O}_2$. The severity in prevalent microcracks, rapid growth of resistance over cycling as well as aging, and CO_2 gas release upon charge to 4.4 V supports the degradation of 4 μm P3-type $\text{Na}_{0.76}\text{Ni}_{0.38}\text{Mn}_{0.62}\text{O}_2$ driven by parasitic surface reactions causing capacity fade.

KEYWORDS: sodium-ion batteries, P3-type, P2-type, secondary particle size, moisture sensitivity, microcracks



INTRODUCTION

In recent years, interest in sodium-ion batteries (SIBs) has considerably increased for low-cost and sustainable energy storage systems as a possible alternative to lithium-ion batteries (LIBs).^{1,2} Among positive electrode materials in SIBs, layered sodium nickel manganese oxides ($\text{Na}_x\text{Ni}_y\text{Mn}_{1-y}\text{O}_2$) and their derivatives have been extensively investigated due to the high capacity delivered by $\text{Ni}^{2+/4+}$ redox couples.^{3–7} However, inferior structural integrity caused by phase transformations and notable surface-electrolyte reactivity with Ni often lead to a capacity fade over cycling. To suppress these issues, partial substitution of element(s) for Ni and/or Mn,^{8–12} surface coating,^{13,14} and morphology altering^{15,16} have been applied. In LIBs, tuning the morphology for layered lithium cathode materials, $\text{LiNi}_x\text{Mn}_y\text{Mn}_z\text{O}_2$ (NMC, $x + y + z = 1$) has shown enhanced electrochemical performance. For example, single-crystal NMC in micron size reduces parasitic surface reaction and particle cracking, leading to improved cycle life.^{17–19} Spherical secondary particles of micron scale, composed of primary nanoparticles, are also beneficial to long-life electrochemical properties because the hierarchical morphology suppresses the detrimental surface reactions while preserving ionic and electronic conductivity thanks to smaller primary

particles.²⁰ These advantages are expected to be efficient in enhancing the properties of sodium layer oxides for SIBs; however, only a few studies have been carried out.

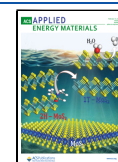
In this report, we focused on the synthesis of $\text{Na}_{0.76}\text{Ni}_{0.38}\text{Mn}_{0.62}\text{O}_2$ with the secondary particle size of 4 and 10 μm , adopting a P2 or P3 phase²¹ (Figure 1) to investigate the influences of secondary particle size and polytype on electrochemical properties. Although high-voltage reactions beyond 3.8 V result in unsatisfactory cyclability irrespective of secondary particle sizes and polytypes, P3-type materials exhibit superior rate capability and cycle life compared to P2-type ones. Using P3-type materials, the mechanism of more pronounced capacity fade for the 4 μm materials in the voltage range 1.6–4.4 V is studied. The results suggest that the morphology degradation in both primary and secondary particles, formed beyond 3.8 V, accelerates electrolyte penetration into the particle interior and

Received: September 29, 2023

Revised: January 7, 2024

Accepted: January 8, 2024

Published: February 1, 2024



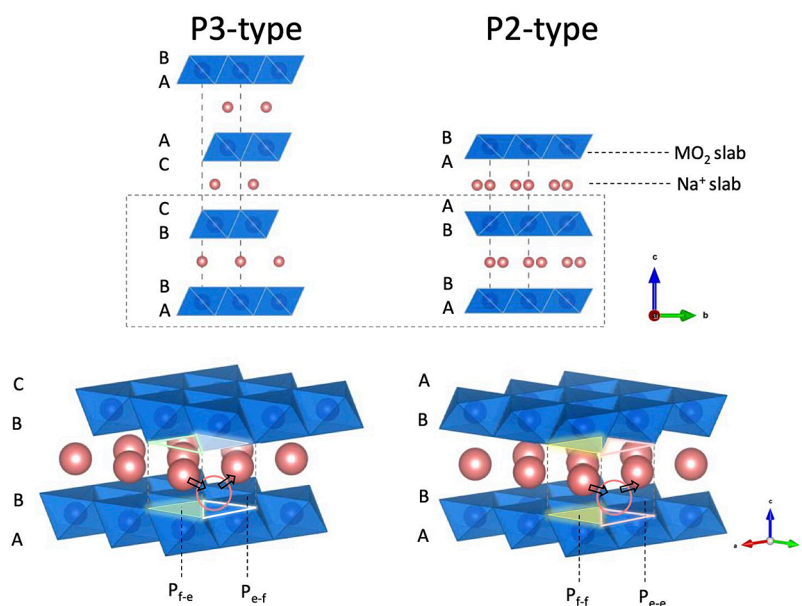


Figure 1. Schematic illustrations of P3- and P2-type structures. In the P3-type structure, the number of MO_2 slabs is three and Na^+ occupy trigonal prismatic sites in a unit cell with the AB BC CA oxygen array stacking along the c -axis. There are crystallographically equivalent trigonal prismatic Na^+ sites, sharing a face with MO_2 at one side and sharing edges with MO_2 at another side (P_{f-e} in green). For convenience, the energetically same Na^+ sites and inverted along the c -axis is called P_{e-f} (white). The Na diffusion repeatedly involves $\text{P}_{f-e} \rightarrow \text{P}_{e-f} \rightarrow \text{P}_{f-e}$ as P_{f-e} is the nearest neighbor to P_{e-f} and vice versa. In the P2-type structure, the number of MO_2 slabs is two and Na^+ occupy trigonal prismatic sites in a unit cell with the AB BA oxygen array stacking along the c -axis. The local environment of the Na^+ sites in this structure is distinguishable. The one called P_{f-f} (yellow) shares faces with MO_2 , and the other one denoted P_{e-e} (pink) shares edges with MO_2 . The Na diffusion pathway is $\text{P}_{f-f} \rightarrow \text{P}_{e-e} \rightarrow \text{P}_{f-f}$ as P_{f-f} is the nearest neighbor to P_{e-e} , and vice versa. The Na diffusion pathway is shown in black arrows, and a diffusion barrier is thought to be lower for the $\text{P}_{f-e} \rightarrow \text{P}_{e-f}$ and $\text{P}_{e-f} \rightarrow \text{P}_{f-e}$ in P3 compared to $\text{P}_{f-f} \rightarrow \text{P}_{e-e}$ and $\text{P}_{e-e} \rightarrow \text{P}_{f-f}$ in P2 by considering possible reposition between cations.

eventually leads to the degradation of active materials, which is more detrimental for the material with a smaller secondary particle size.

EXPERIMENTAL SECTION

Material Synthesis. Transition metal hydroxide precursors ($\text{Ni}_{0.38}\text{Mn}_{0.62}$)(OH)₂ with secondary particle sizes 4 and 10 μm in diameter, synthesized by coprecipitation, were provided by Umicore. Considering the typical composition and valence of $\text{Na}_{2/3}[\text{Ni}(\text{II})_{1/3}\text{Mn}(\text{IV})_{2/3}]\text{O}_2$, the molar ratio of Ni : Mn = 0.38 : 0.62 is selected to slightly increase the Na content while keeping the P3 or P2 structure in the final products. Powder X-ray diffraction (PXRD) patterns and particle size distributions, using a Partica mini LA-350 (Horiba), of the precursors were checked prior to use (Figure S1). The ($\text{Ni}_{0.38}\text{Mn}_{0.62}$)(OH)₂ precursors were thoroughly mixed with a stoichiometric equivalent of sodium carbonate (Na_2CO_3 , Nacalai Tesque, 99.8%) for the nominal composition of $\text{Na}_{0.76}\text{Ni}(\text{II})_{0.38}\text{Mn}(\text{IV})_{0.62}\text{O}_2$ using a mortar and a pestle. The mixed powders were heated at 700, 800, and 900 $^\circ\text{C}$ in air for 14 h with a heating rate of 5 $^\circ\text{C min}^{-1}$ and then quenched directly into an Ar-filled glovebox. Of note, a slightly higher temperature^{22–25} is applied to achieve a highly crystalline P3 phase and quenching^{26–28} is applied to avoid vacancies in transition metal layers. The nomenclature of samples is given in Table 1.

As-Prepared Material Characterization. PXRD patterns were recorded on a Rigaku SmartLab equipped with a Cu K α radiation source with a Ni filter using a homemade airtight sample holder. Scanning electron microscopy (SEM, JCM-6000 or JSM-7001F, JEOL) was applied to observe particle morphology. Moisture sensitivity was tested using a temperature and humidity chamber, Yamato IW223.

Electrode Preparation. To prepare slurries, 80 wt % active material, 10 wt % acetylene black (Strem Chemicals), and 10 wt % poly(vinylidene fluoride) (PVDF, Polyscience) were mixed in *N*-methyl-2-pyrrolidone. The slurry was casted on aluminum foil using a doctor blade and dried at 150 $^\circ\text{C}$ under vacuum. The electrode preparation was carried out in an Ar-filled glovebox.

Table 1. Nomenclature of the As-Prepared Samples Using ($\text{Ni}_{0.38}\text{Mn}_{0.62}$)(OH)₂ Precursors

	heating temperature ($^\circ\text{C}$)	secondary particle size of precursor (μm)
NiMn-4-700	700	4
NiMn-4-800	800	
NiMn-4-900	900	
NiMn-10-700	700	10
NiMn-10-800	800	
NiMn-10-900	900	

Electrochemical Test. Coin cells (R2032, Hosen) and three-electrode cells (TYS-00DM02D, Toyo System) were assembled in an Ar-filled glovebox. The cells were made of a disk electrode, sodium metal (Kanto Chemical) as counter/reference electrodes, and a glass fiber separator (Advantec, GB-100R) soaked in the electrolyte (1 M sodium hexafluorophosphate (NaPF_6) in propylene carbonate (PC), Kishida) with 2 vol % fluoroethylene carbonate (FEC, Kishida) as the electrolyte additive. Galvanostatic charge/discharge cycling and the galvanostatic intermittent titration technique (GITT) were carried out using a TOSCAT-3100 (Toyo System) at 25 $^\circ\text{C}$. Electrochemical impedance spectroscopy (EIS) was performed in a frequency range from 1 MHz to 10 mHz with an AC signal amplitude of 10 mV using a VMP3 (Biologic) at 25 $^\circ\text{C}$.

Online Electrochemical Mass Spectrometry (OEMS). OEMS measurements were performed using a custom-ordered OEMS cell (EC Frontier) assembled in an Ar-filled glovebox. The cell consists of a working electrode (15 mm in diameter) and sodium metal (15 mm in diameter) as counter/reference electrodes. The electrodes were separated by a glass fiber separator and soaked with 400 μL of the electrolyte mentioned above. The cells were charged to 4.4 V at a rate of 12.5 mA g^{-1} (C/20) at 25 $^\circ\text{C}$. The cell was connected to an SP-150 (Biologic) and a gas chromatograph–mass spectrometer (GCMS-QP2020 NX in a columnless configuration, Shimadzu) without

exposure to ambient air, enabling simultaneous electrochemical and MS measurements (quadrupole detector). He (99.99995%) was used as the carrier gas. All mass signals were normalized by the measured intensity at $m/z = 219$ for a standard sample of perfluorotributylamine before each experiment, i.e., autotuning, facilitating a numerical comparison of the intensity signals for different experiments. For $m/z = 32$ (O_2) and 44 (CO_2), the system was calibrated to ensure complete quantitative measurements. Calibrations were conducted by using standard gases; mixed gases were allowed to flow into the MS through a separate line. O_2 and CO_2 concentrations were controlled by varying the ratio of mixed gas and pure He, and MS intensities of all concentrations were recorded. Based on this relation, calibration curves were generated.

Postmortem Analysis. Cycled electrodes were extracted from the rest of the cells and washed carefully with dimethyl carbonate (DMC, Kishida) without air exposure and then dried under a vacuum. Ex situ XRD patterns and SEM images were obtained using the aforementioned equipment. For cross-sectional SEM images, JEOL IB-19520CCP was used to polish electrodes.

RESULTS AND DISCUSSION

Characterization of the As-Prepared Materials. PXRD patterns of the six samples synthesized using the precursors are shown in Figure 2. All peaks in NiMn-4-700 and NiMn-10-700

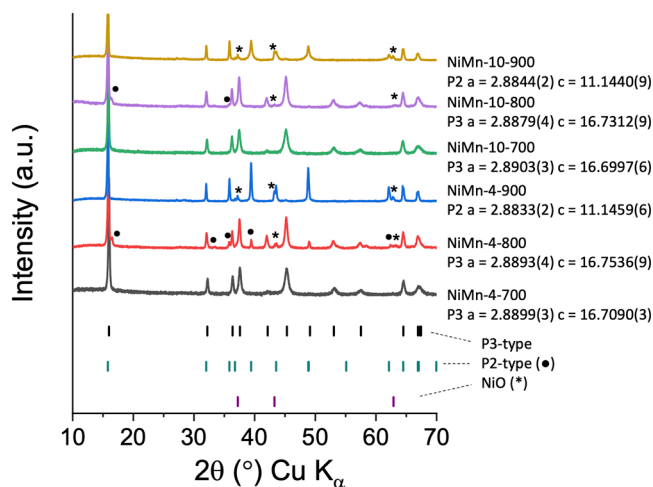


Figure 2. PXRD patterns of the six samples prepared using $(Ni_{0.38}Mn_{0.62})(OH)_2$ with secondary particle sizes 4 and 10 μm in diameter. Tick marks in black indicate allowed reflections for NiMn-4-700 using a P3-type structure (space group of $R3m$). Tick marks in dark cyan and purple indicate allowed reflections for NiMn-4-900 using the P2-type structure (space group of $P6_3/mmc$) and NiO impurity, respectively.

can be indexed on the P3-type structure using space group $R3m$ without obvious impurities. Heating at 800 $^{\circ}C$ (NiMn-4-800 and NiMn-10-800) produces a second phase adopting the P2-type structure (space group of $P6_3/mmc$) and NiO impurity, while major peaks can be indexed on the P3-type structure. Tentative phase fraction refinements suggest 7.8 (5) and 1.7 (5) wt % of the P2-type structure for NiMn-4-800 and NiMn-10-800, respectively, and negligible NiO fraction. Heating at 900 $^{\circ}C$ stabilizes the P2-type structure as shown in NiMn-4-900 and NiMn-10-900, where NiO impurity exists as well. A similar amount of NiO (about 9.1 and 11.9 wt % for NiMn-4-900 and NiMn-10-900, respectively) barely affects any difference between the two samples owing to the NiO impurity. These results demonstrate that the crystallization and polytype of $Na_{0.76}Ni_{0.38}Mn_{0.62}O_2$ are simply dependent on the heating temperature. Comparing refined cell parameters (Table 2) using

Table 2. Refined Cell Parameters and Interlayer Distance ($d_{interlayer}$) for the Major Phase

	major phase	$a = b$ (\AA)	c (\AA)	$d_{interlayer}$ (\AA)
NiMn-4-700	P3	2.8899(3)	16.7090(3)	5.5697(1)
NiMn-4-800	P3	2.8893(4)	16.7536(9)	5.5845(4)
NiMn-4-900	P2	2.8833(2)	11.1459(6)	5.5730(3)
NiMn-10-700	P3	2.8903(3)	16.6997(6)	5.5666(3)
NiMn-10-800	P3	2.8879(4)	16.7312(9)	5.5771(4)
NiMn-10-900	P2	2.8844(2)	11.1440(9)	5.5720(4)

GSAS-II²⁹ between NiMn-4-700 and NiMn-4-900 reveals the shortening of the in-plane Mn(Ni)-O bond distances (a -axis) and elongated interlayer distances ($Mn(Ni)O_2$ - $Mn(Ni)O_2$) probably due to relatively severe volatilization of sodium at the higher heating temperature, leading to the smaller ion size of oxidized Ni and Mn, and electrostatic repulsion of MO_2 slabs, respectively. The trend in the cell parameters is identical for the 4 and 10 μm samples, implying negligible effects of particle size on thermodynamically stable polytypes and sodium volatilization at the higher temperature.

For the samples heated at 700 and 900 $^{\circ}C$, further characterization was carried out. SEM images of precursors and the four samples adopting the P3 or P2 phase are shown in Figure 3. Both precursors exhibit nearly spherical secondary particles 4 and 10 μm in diameter. The 4 μm ($Ni_{0.38}Mn_{0.62})(OH)_2$ precursor (Figure 3a) consists of thin plate-like primary particles (about 100 nm in thickness), whereas the 10 μm ($Ni_{0.38}Mn_{0.62})(OH)_2$ precursor (Figure 3d) is composed of thicker barlike primary particles (about 1 μm in thickness), more tightly packed into the hierarchical sphere. The heating process maintains the secondary particle size. However, primary particles tend to enlarge as the heating temperature is higher; NiMn-4-900 (Figure 3c) displays a larger hexagonal platelet morphology with a thickness of 200–400 nm than NiMn-4-700 (Figure 3b) with particle thickness of 100–150 nm. The trend is similar to the synthesis of NMC as reported.^{30,31}

In general, layered sodium metal oxides (Na_xMeO_2) are sensitive to moisture.³² To examine moisture sensitivity as a function of secondary particle size and polytype, the four powders of NiMn-4-700, NiMn-4-900, NiMn-10-700, and NiMn-10-900 were kept in glass vials covered with pierced aluminum foil at 25 $^{\circ}C$ and relative humidity (RH) of 90%. PXRD patterns measured after 1 day and 7 days are shown in Figure 4. No hydrate phase emerges even after a week for NiMn-4-900 and NiMn-10-900, whereas the hydrate phase is observed after a day for NiMn-4-700 and NiMn-10-700. Table 3 displays refined cell parameters based on P3 and P2 types. For all samples, the lattice parameter c increases during storage. Indeed, the enlargement of c is more significant as the storage day is prolonged for P3-type materials (NiMn-4-700 and NiMn-10-700), whereas no obvious increase is found for P2-type materials (NiMn-4-900 and NiMn-10-900). The changes in c is probably associated with Na^+/H^+ exchange, which is often observed in O3-type sodium transition metal oxides.^{33,34} We believe the slightly broad peaks after a day for P3-type samples are attributed to stacking faults.³⁵ This result implies less moisture sensitivity for P2-type samples over P3-type samples, consistent with the previous report.³⁶ Interestingly, the hydrate phase is more obvious in NiMn-4-700 than in NiMn-10-700, suggesting that the degradation caused by humidity is more severe with a large surface area.

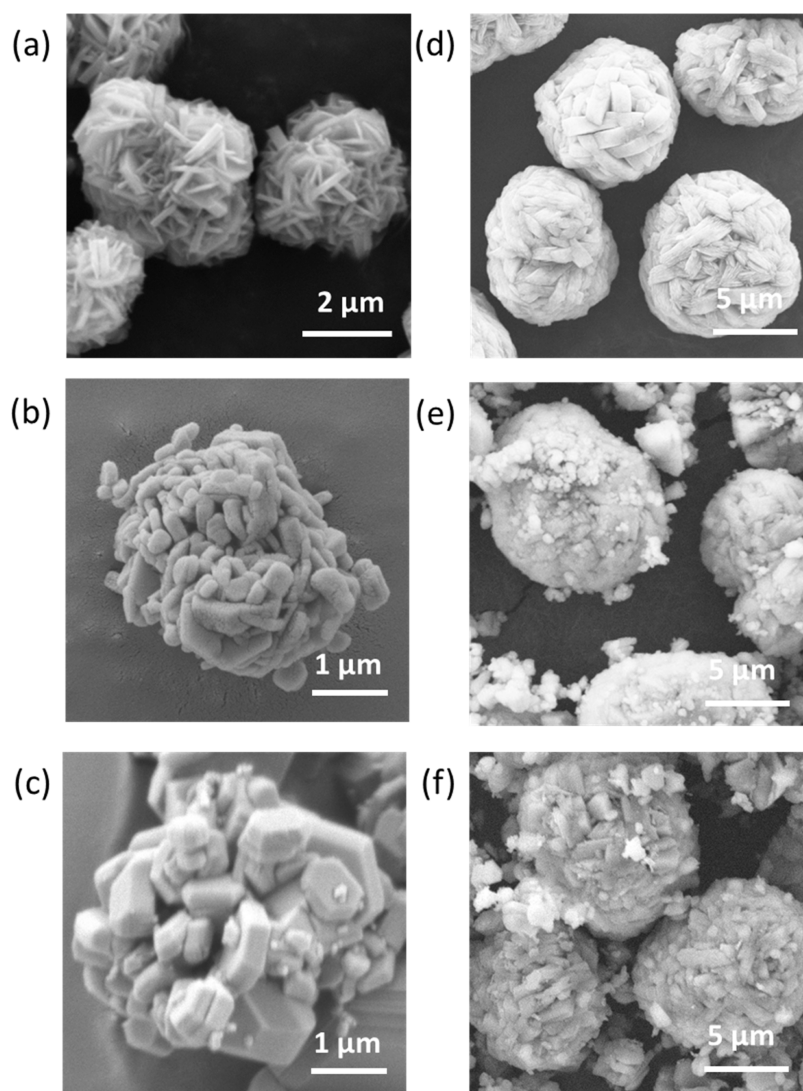


Figure 3. SEM images of (a) $4\ \mu\text{m}$ $(\text{Ni}_{0.38}\text{Mn}_{0.62})(\text{OH})_2$, (b) NiMn-4-700, (c) NiMn-4-900, (d) $10\ \mu\text{m}$ $(\text{Ni}_{0.38}\text{Mn}_{0.62})(\text{OH})_2$, (e) NiMn-10-700, and (f) NiMn-10-900.

Electrochemical Properties in Various Voltage Ranges. To examine redox stability depending on polytypes and voltage ranges, nonaqueous Na cells of NiMn-10-700 and NiMn-10-900 were assembled and cycled galvanostatically at $25\ \text{mA g}^{-1}$ ($C/10$) in four different voltage ranges of 1.6–4.4, 2.5–4.4, 1.6–3.8, and 2.5–3.8 V. Charge/discharge profiles of every five cycles are shown in Figure 5. In the widest voltage range of 1.6–4.4 V (Figure 5a,e), both polytypes show analogous load curves beyond 2.5 V with a long plateau at 4.2 V on the first cycle, attributed to the structural transformations of P3–O₃^{37–39} (Figure S2a) and P2–O₂^{40,41} (Figure S2b) for NiMn-10-700 and NiMn-10-900, respectively. Below 2.5 V, the P3-type material (NiMn-10-700) exhibits a flat plateau at 2.0 V, whereas the P2-type material (NiMn-10-900) demonstrates a sloping plateau instead, where structural changes of P3–O₃ (Figure S2a) and P2–P'2 (Figure S2b) occur for P3-type and P2-type materials, respectively. In this voltage range, the capacity fades significantly, delivering only $109.2\ \text{mAh g}^{-1}$ (50% of initial capacity) for NiMn-10-700 and $84.5\ \text{mAh g}^{-1}$ (39% of initial capacity) for NiMn-10-900 after 60 cycles (Figure S3). The repeated phase changes over cycling accumulate lattice stress and cause particle cracks, leading to

capacity fade as commonly observed in Na_xMeO_2 .^{42,43} In addition, Mn^{3+} (Jahn–Teller distortion ion) is formed in the low-voltage region and can undergo a disproportionation reaction forming Mn^{4+} and Mn^{2+} .^{44,45} The Mn^{2+} is known to dissolve into the carbonate-based electrolyte, which can also affect cyclability.

When the lower cutoff voltage is set at 2.5 V (Figure 5b,f), slight enhancement in capacity retention is observed with the capacity retention of 57.4 and 51% for NiMn-10-700 and NiMn-10-900, respectively, at the expense of initial capacity. Decreasing the upper cutoff voltage to 3.8 V (Figure 5c,g) shows stable redox reversibility, delivering $137.2\ \text{mAh g}^{-1}$ (capacity retention of 89.6%) and $120.4\ \text{mAh g}^{-1}$ (capacity retention of 83.2%) for NiMn-10-700 and NiMn-10-900, respectively, after 60 cycles. In the 2.5–3.8 V range without structural evolution (Figure 5d,h), a much-improved cycling performance is observed with discharge capacities of 81.3 and $73.7\ \text{mAh g}^{-1}$ at cycle 60 for NiMn-10-700 and NiMn-10-900, respectively. The results in four voltage ranges reveal that (i) the P3-type material delivers slightly higher initial capacity than the P2-type material, (ii) the capacity retention of the P3-type material is superior to that of the P2-type one, and (iii) reactions

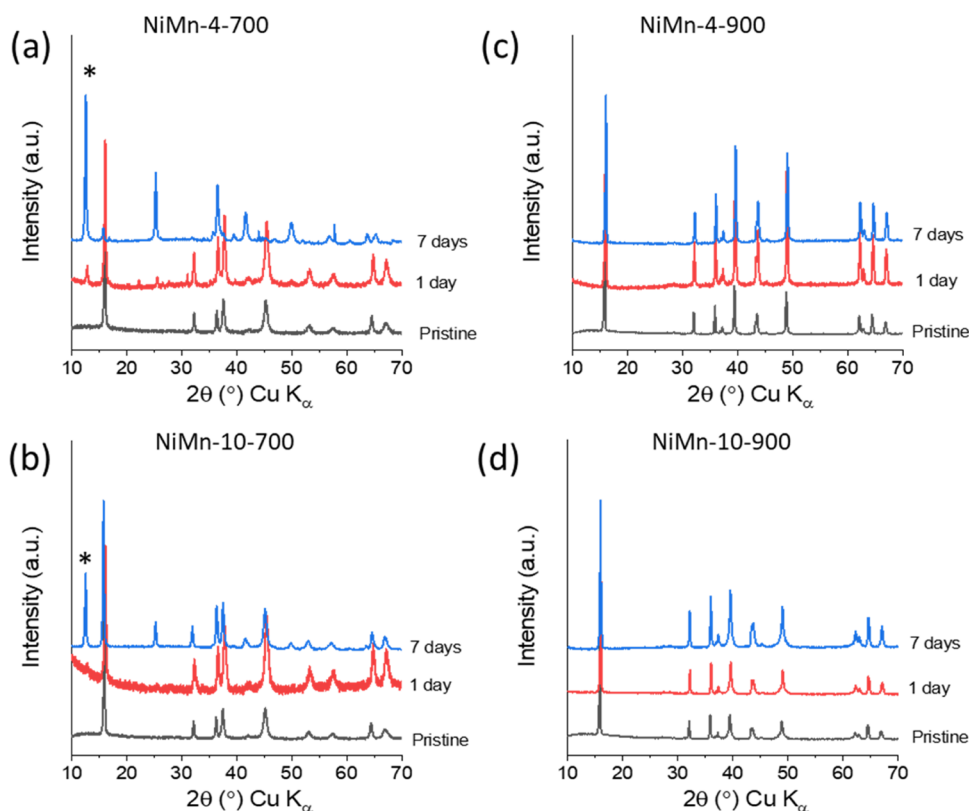


Figure 4. PXRD patterns of (a) NiMn-4-700, (b) NiMn-10-700, (c) NiMn-4-900, and (d) NiMn-10-900 kept at 25 °C and relative humidity (RH) of 90% for a day (red) and 7 days (blue) in comparison with pristine (black) ones. The asterisk represents the hydrate phase.

Table 3. Refined Cell Parameters

		pristine		1 day		7 days	
		<i>a</i> = <i>b</i> (Å)	<i>c</i> (Å)	<i>a</i> = <i>b</i> (Å)	<i>c</i> (Å)	<i>a</i> = <i>b</i> (Å)	<i>c</i> (Å)
P3	NiMn-4-700	2.8899(3)	16.7090(3)	2.8820(4)	16.763(3)	2.874(7)	16.90(7)
	NiMn-10-700	2.8903(3)	16.6997(6)	2.8861(5)	16.767(4)	2.8811(6)	16.779(5)
P2	NiMn-4-900	2.8833(2)	11.1459(6)	2.8867(3)	11.165(1)	2.8851(3)	11.160(1)
	NiMn-10-900	2.8844(2)	11.1440(9)	2.8838(3)	11.150(1)	2.8851(4)	11.15(1)

related to the phase transitions and electrolyte decomposition beyond 3.8 V jeopardize cycle life for both polytypes. The inferior electrochemical properties of P2-type materials might be attributed to NiO impurity as it is a poor electronic conductor⁴⁶ and has limited diffusion paths for ionic transport⁴⁷ as a rock salt structure and larger primary particles that can suffer from the stress induced by lattice volume changes.⁴⁸

Galvanostatic cycling tests of the 4 μm samples were conducted for NiMn-4-700 and NiMn-4-900 in two voltage ranges of 1.6–4.4 and 1.6–3.8 V to examine the effects of secondary particle size on electrochemical properties. Load curves for the 4 μm samples adopting P3 and P2 types are shown in Figure 6a–d, where no discernible influence of the particle size is found on the first cycle, delivering similar initial capacity and voltage curves to those of 10 μm samples in both voltage ranges. Indeed, NiMn-4-700 (Figure S4) exhibits structural evolutions beyond 3.8 V and below 2.5 V, which are identical to those of NiMn-10-700 (Figure S2a). However, the materials with the secondary particle size of 4 μm result in a more pronounced capacity fade in both polytypes, especially in the voltage range of 1.6–4.4 V (Figure 6e,f). This hints that active material degradation driven by surface reactions might play a crucial role in capacity fade.

Capacity Fade Mechanism on P3-Type Materials. P3-type materials (NiMn-4-700 and NiMn-10-700) are selected to understand the capacity fade mechanism as a function of secondary particle size, as they demonstrate superior electrochemical properties than P2-type materials. It has been shown that the capacity fade of layered oxides in SIBs is attributed to structural transformations. For example, irreversible structural changes beyond certain upper cutoff voltage cause unsatisfactory cycle stability as reported in O'3-type NaMnO₂ and O3-type NaCrO₂.^{49,50} Despite relatively reversible structural evolution, lattice volume change due to different phases as well as repeated lattice volume changes in 1.6–4.4 V can contribute to structural degradation, eventually forming microcracks.⁵¹ Lattice volume was calculated from ex situ XRD patterns (Figures S2, S4, and S5), as shown in Figure 7. On the first cycle, lattice volume reduction is almost negligible after charge to 3.8 V (CH 3.8 V) for both samples, maintaining the pristine P3 phase. In contrast, the P3–O3 structural evolution in NiMn-4-700 and NiMn-10-700 induces ca. 22 and 18% lattice volume contraction, respectively, from pristine state to that after charge to 4.4 V (CH 4.4 V). Subsequent discharge to 1.6 V results in lattice expansion with lattice volumes of 121.97(1) Å³ and 121.58(1) Å³ for NiMn-4-700 and NiMn-10-700, respectively. After 100

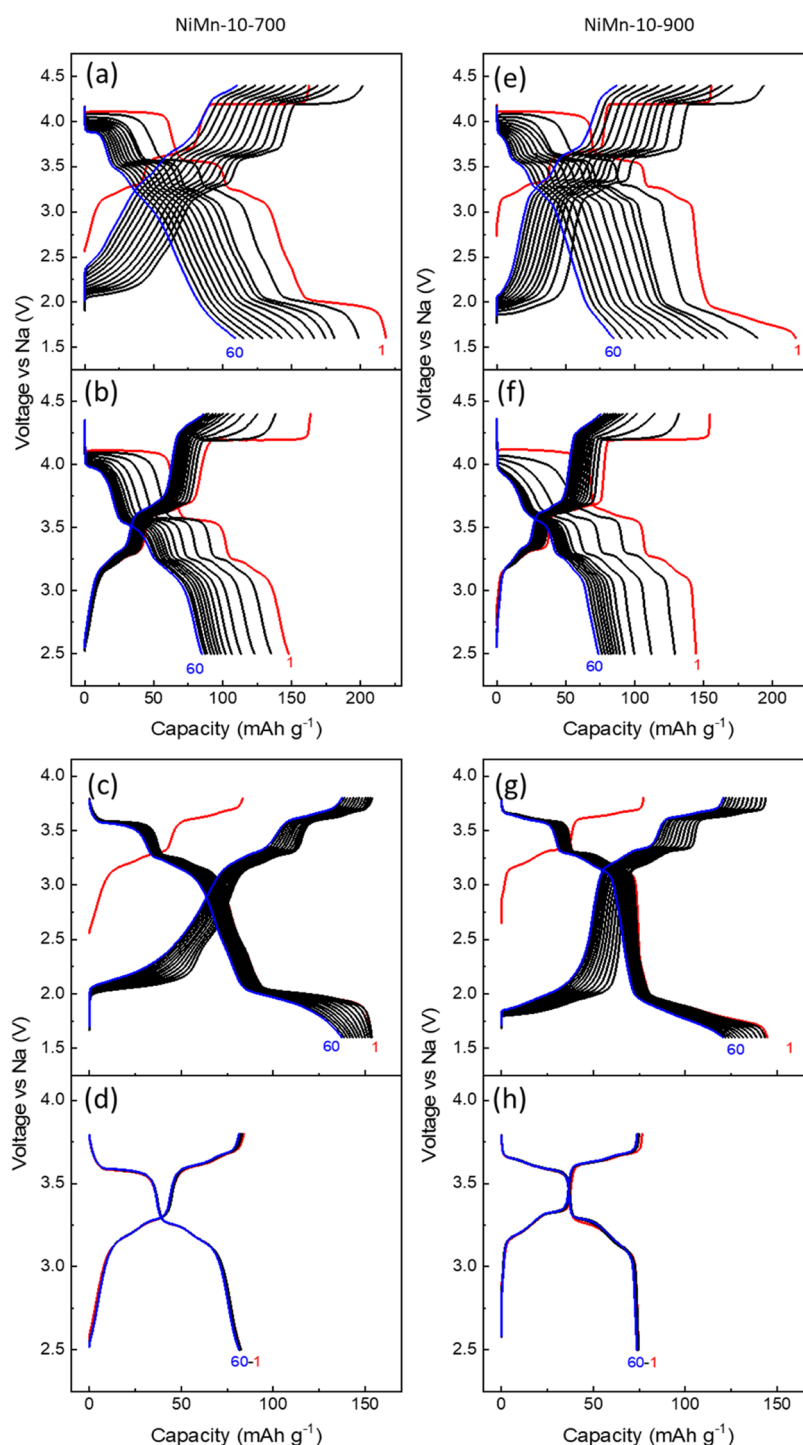


Figure 5. Charge/discharge profiles of every five cycles for (a–d) NiMn-10-700 and (e–h) NiMn-10-900 cycled at 25 mA g^{-1} (C/10) in the voltage ranges of 1.6–4.4, 2.5–4.4, 1.6–3.8, and 2.5–3.8 V. Red and blue curves indicate cycle 1 and cycle 60, respectively.

cycles in 1.6–4.4 V, both NiMn-4-700 and NiMn-10-700 exhibit the P'3 phase with lattice volumes of $79.19(6)$ and $80.71(3) \text{ \AA}^3$, corresponding to 35.1 and 33.6% volume contraction from the first cycle. Lowering the upper cutoff voltage to 3.8 V leads to the dominant O3 phase even after 100 cycles for NiMn-4-700 with no obvious lattice volume change. This suggests that degradation of active material in bulk occurs beyond 3.8 V, leading to capacity fade over cycling.

Since those lattice volume changes would induce microcracks on particles, cross-sectional SEM images of NiMn-4-700 and

NiMn-10-700 at different states were recorded (Figure 8). At pristine electrodes, NiMn-4-700 features some pores between primary particles (within secondary particles), whereas NiMn-10-700 shows pores only in the center of secondary particles, and primary particles are tightly packed. After the charge reaches 3.8 V, no obvious microcracks are found for both NiMn-4-700 and NiMn-10-700, in agreement with no obvious lattice volume change. Subsequent charge to 4.4 V develops microcracks in the secondary particle (yellow arrows), which are more pronounced for NiMn-10-700. After discharge to 1.6 V shown in Figure 8d,8i

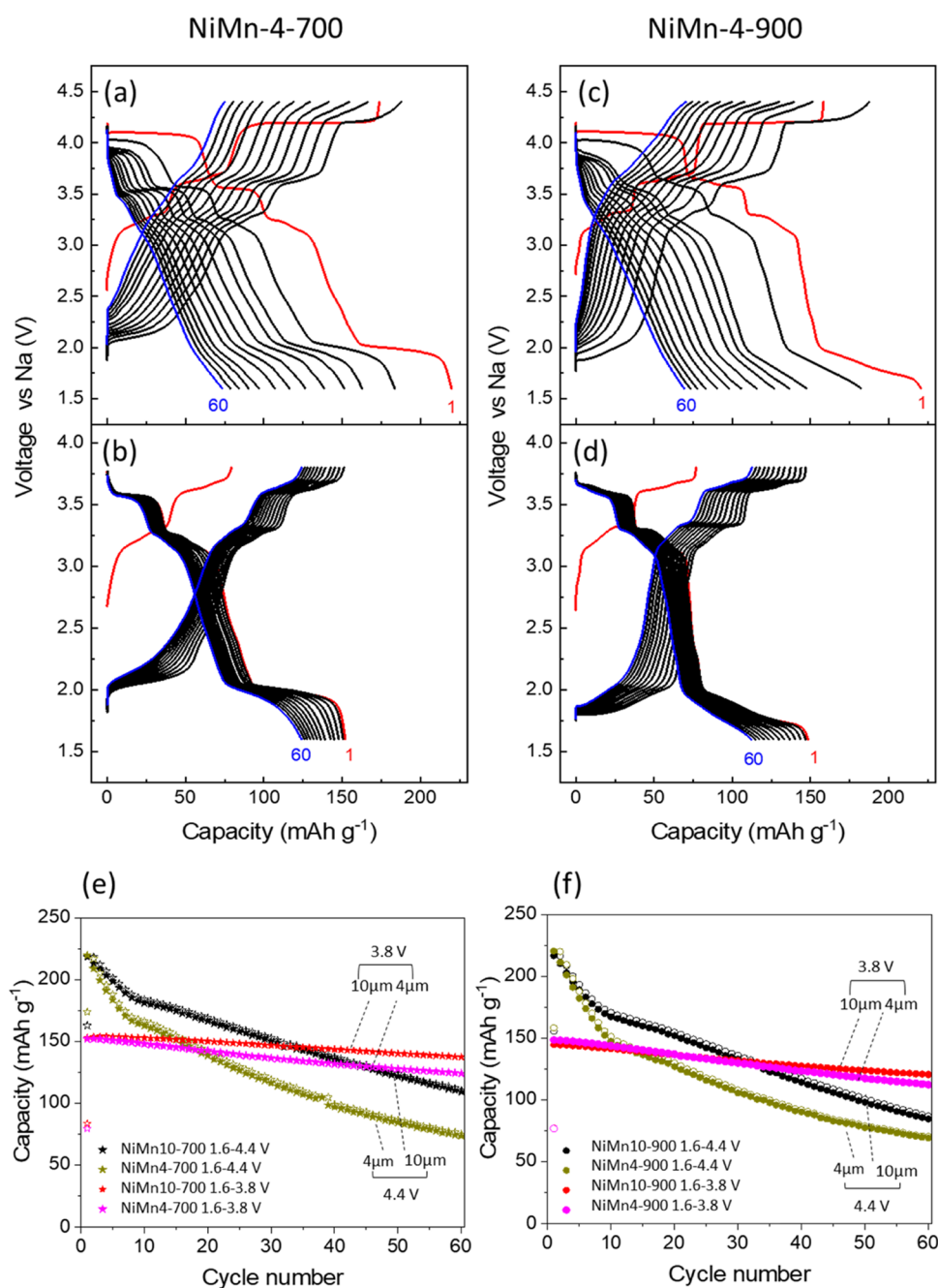


Figure 6. Charge/discharge profiles of every five cycles for (a, b) NiMn-4-700 and (c, d) NiMn-4-900 cycled at 25 mA g^{-1} ($C/10$) in the voltage ranges of 1.6–4.4 and 1.6–3.8 V. Red and blue curves indicate the first and 60th cycle, respectively. Cyclability for (e) P3-type materials and (f) P2-type materials having secondary particle sizes of 4 and $10 \mu\text{m}$. Empty and full symbols indicate the charge and discharge capacity, respectively.

(CYC1), the gaps between primary particles (red arrows) become large for NiMn-4-700 along with more developed microcracks in the secondary particle, and NiMn-10-700 shows more pronounced microcracks in the secondary particles. After 100 cycles in the voltage range of 1.6–4.4 V, intraparticle microcracks in the primary particles (light blue arrow) are additionally found for both NiMn-4-700 and NiMn-10-700. Furthermore, microcracks in the secondary particles are much more pronounced in the NiMn-4-700 sample, which agrees with the better capacity retention in NiMn-10-700, as shown in Figure 6e. In the case of NiMn-4-700, the gaps between the primary particles also severely expand. These results can be reconciled with the evolution of lattice volume, namely, the

more significant lattice volume change in NiMn-4-700 (Figure 7) induces more degradation of secondary and primary particles due to mechanical stress on the first cycle as well as the accumulated stress over repeated volume changes. Cross-sectional SEM images after 100 cycles in 1.6–3.8 V clearly show mitigated particle degradation, as shown in Figure S6, confirming the correlation between the lattice volume change and the origin of pulverization of secondary particles and intraparticle microcracks. Therefore, it is believed that NiMn-4-700 allows more infiltration of the electrolyte, leading to more pronounced active material degradation beyond 3.8 V.

Furthermore, impedance measurements for NiMn-4-700 and NiMn-10-700 were carried out after the first charge (1st CH 4.4

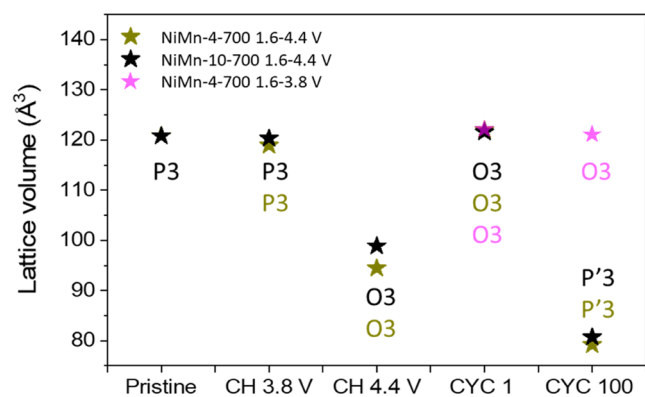


Figure 7. Calculated lattice volume at different states for NiMn-4-700 and NiMn-10-700. Major phases are shown for each state. CYC1 and CYC100 indicate the state after the first cycle and 100th cycle, respectively, between 1.6 and 4.4 V.

V) and the 30th charge to 4.4 V (30th CH 4.4 V), as well as over aging for 14 days in an open circuit (Figure S7) after the 30th charge (aging 1 day, aging 7 days, and aging 14 days). As shown in Figure 9a,9b and Table S1, total resistance, i.e., fitted result for the semicircle, of NiMn-10-700 (107.9 Ω) is slightly lower than that of NiMn-4-700 (128.8 Ω) after the first charge. After the 30th charge, notable growth in impedance is found for both samples, and the increase is more significant for NiMn-4-700. In addition, the impedance build-up over 14 days is more rapid in NiMn-4-700. These results suggest that the surface degradation is more serious as secondary particles are smaller.

To observe CO_2 and O_2 gas evolution as a function of time during charge to 4.4 V at C/20, OEMS measurements were performed for NiMn-4-700 and NiMn-10-700 (Figure 9c,d). O_2 gas evolution is not detected for both samples upon charge, while CO_2 gas releases beyond 4.1 V. The absence of O_2 gas release cannot conclude any lattice O loss since a major fraction of released lattice O would react with solvents in the electrolyte, which is predominantly detected as CO_2 .^{52–54} Therefore, examining CO_2 signals is more important; the maximum amount of evolved CO_2 is 1.0 $\text{mmol min}^{-1} \text{mg}^{-1}$ for NiMn-4-700 and 0.6 $\text{mmol min}^{-1} \text{mg}^{-1}$ for NiMn-10-700 at 4.2 V. This reveals that the smaller secondary particles cause the more detrimental side reactions.⁵⁵

Additionally, TEM EDS measurements (Figure S8) were performed for NiMn-4-700 and NiMn-10-700, assuming that Na residues might be formed as Na_2CO_3 .⁵⁶ The results reveal that no Na_2CO_3 is found on the surface of both samples. This means no impact of surface residue on the capacity fade. Instead, the severe detrimental reactions with the electrolyte due to the smaller secondary particle size govern the capacity fade, as observed from the DEMS data.

Electrochemical Properties at Various Rates. To understand the effects of secondary particle size and polytype on rate capability, a series of five cycles in the voltage range of 1.6–3.8 V at progressively increasing discharge rates from C/10 to 2C, keeping the charge rate at C/10, was performed for NiMn-10-700, NiMn-10-900, NiMn-4-700, and NiMn-4-900. As shown in Figures 10a and S9a–d, NiMn-4-700 shows the best rate capability among the four samples, delivering 128.4 mAh g^{-1} at 2C, equivalent to 83% at C/10. The order of rate capability is NiMn-4-700 \gg NiMn-10-700 > NiMn-4-900 > NiMn-10-900, implying that the P3 phase is beneficial at fast rates compared with the P2 phase, as described in Figure 1. It is

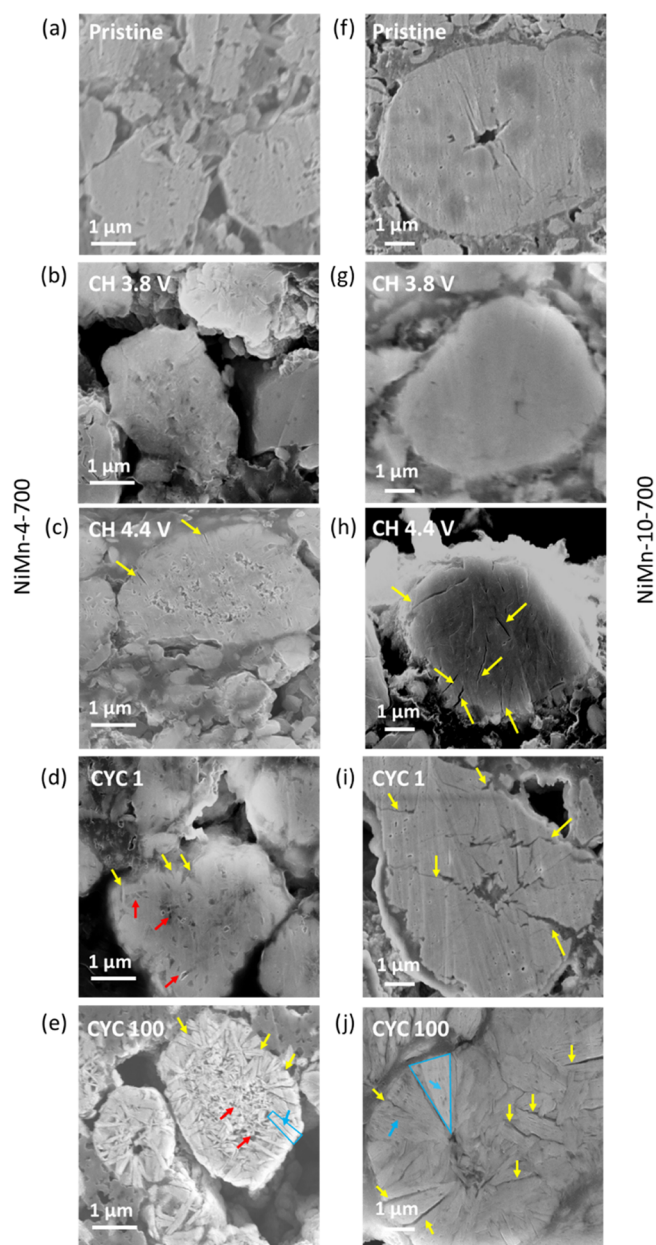


Figure 8. Cross-sectional SEM images of (a–e) NiMn-4-700 and (f–j) NiMn-10-700 at pristine, after charge to 3.8 V (CH 3.8 V), charge to 4.4 V (CH 4.4 V), cycle 1 (CYC1, charge to 4.4 V then discharge to 1.6 V), and cycle 100 (CYC 100, in the voltage range of 1.6–4.4 V) cycled at 25 mA g^{-1} (C/10). Yellow, red, and light blue arrows indicate microcracks in the secondary particles, gaps between primary particles, and intraparticle microcracks in the primary particles, respectively. Light blue lines highlight a primary particle.

suspected that smaller primary particles in P3-type materials would permit superior rate capability because of the increased interfacial area with the electrolyte and shortened Na^+ diffusion length. In addition, the Na^+ diffusion coefficient was determined via GITT profiles, using the same method described in the previous papers^{57,58} (Figure S9e) for NiMn-4-700 and NiMn-4-900, obtained by discharge at C/50 for 0.25 h, followed by 1 h relaxation in the voltage range of 1.6–3.8 V in the three-electrode cells. Since the voltage plateaus regions correspond to biphasic reactions, a comparison of the calculated Na^+ diffusion coefficient (Figure 10b) at solid solution phase transition

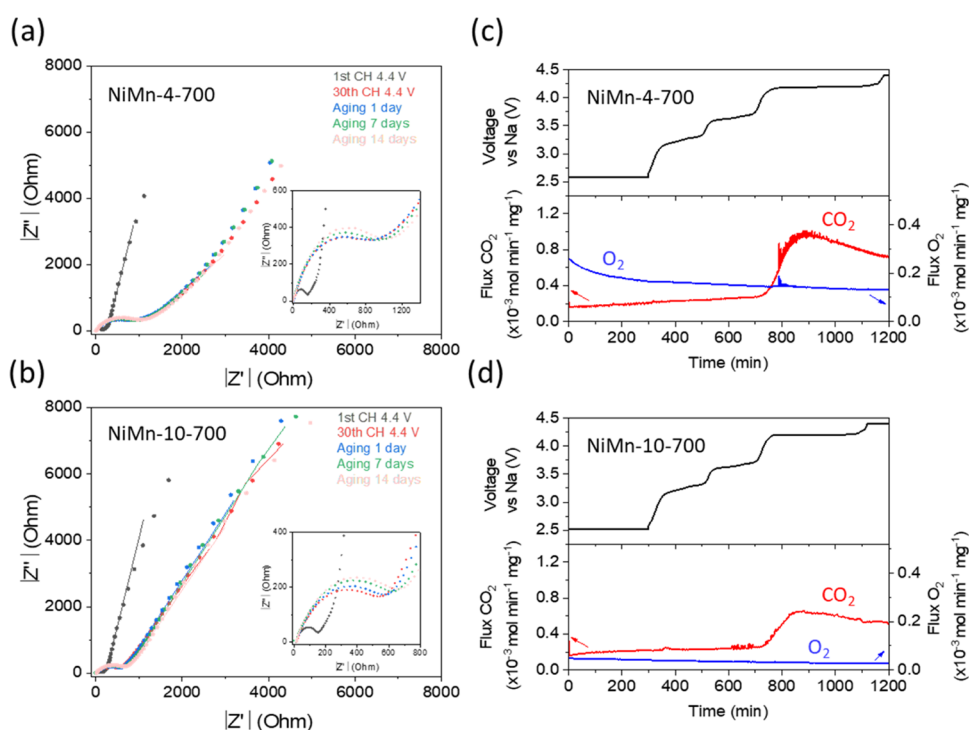


Figure 9. Nyquist plots for (a) NiMn-4-700 and (b) NiMn-10-700, with zoomed-in images for high frequency. Charge profile and gas evolution as a function of time for (c) NiMn-4-700 and (d) NiMn-10-700.

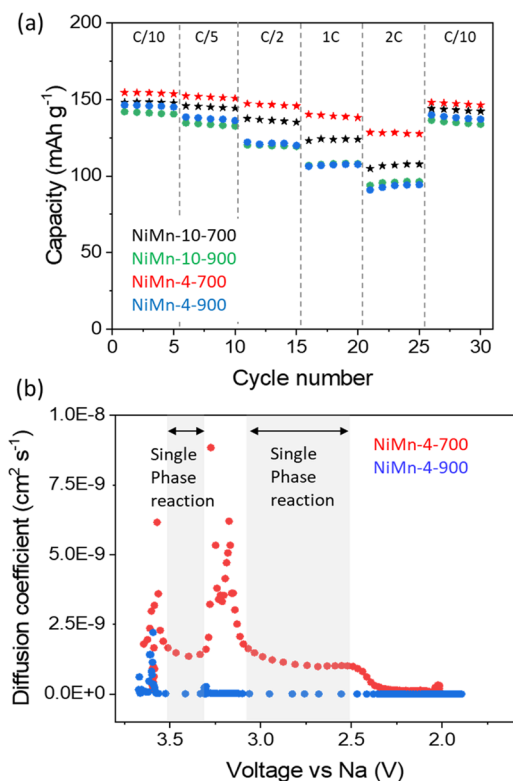


Figure 10. (a) Discharge capacity at various discharge current rates cycled at 1.6–3.8 V. (b) Na⁺ diffusion coefficient determined via GITT profiles, highlighting solid solution phase transition regions in gray.

regions is only reasonable (gray regions) in which NiMn-4-700 shows a higher diffusion coefficient compared with NiMn-4-900. This is due to the lower barrier of sodium diffusion via $P_{Fe} \rightarrow P_{e-f}$ sites in the P3 phase than the one via $P_{ff} \rightarrow P_{e-e}$ sites in the P2

phase, as illustrated in Figure 1. The smaller primary particles and superior diffusion coefficient of NiMn-4-700 enable a better rate capability than NiMn-10-700. It is worth noting that smaller secondary particles jeopardize cycle life, but smaller primary particles are beneficial in rate performance.

CONCLUSIONS

Varying the heat temperature of the mixture of $(Ni_{0.38}Mn_{0.62})-(OH)_2$ precursor and Na_2CO_3 produces P3- and P2-type $Na_{0.76}Ni_{0.38}Mn_{0.62}O_2$ while maintaining the spherical secondary particle morphology of the precursors with a diameter of 4 or 10 μm . P3-type materials (NiMn-4-700 and NiMn-10-700) display smaller primary particles than P2-type counterparts (NiMn-4-900 and NiMn-10-900) and no obvious impurities; however, the resistance against moisture is limited, which is lower in the case of the 4 μm sample compared with the 10 μm one. With respect to electrochemical performance, P3-type and 10 μm show enhanced cyclability over P2-type and 4 μm in the voltage range of 1.6–4.4 V, where parasitic reactions beyond 3.8 V cause notable capacity fade. Ex situ XRD measurements confirm the structural changes of P3–O3 for P3-type and P2–O2 for P2-type materials in the high-voltage region (3.8–4.4 V) for both secondary particle sizes. Cross-sectional SEM images, EIS, and OEMS measurements support that the microcracks formed by the repeated lattice volume change result in the increased exposure of internal particles to the penetrated electrolyte and degrade the active materials. These phenomena are more severe in NiMn-4-700 than in NiMn-10-700, proposing that the degradation of $Na_{0.76}Ni_{0.38}Mn_{0.62}O_2$ driven by surface reactions beyond 3.8 V jeopardizes cycle life.

■ ASSOCIATED CONTENT

SI Supporting Information

The Supporting Information is available free of charge at <https://pubs.acs.org/doi/10.1021/acsaem.3c02462>.

PXRD and particle size distribution for $(\text{Ni}_{0.38}\text{Mn}_{0.62})\text{(OH)}_2$ precursors; ex situ XRD for NiMn-10-700, NiMn-10-900, and NiMn-4-70; capacity vs cycle number for NiMn-10-700 and NiMn-10-900; cross-sectional SEM images for NiMn-4-700 and NiMn-10-700 after 100 cycles between 1.6 and 3.8 V; voltage changes over aging for NiMn-4-700 and NiMn-10-700; total resistance and used equivalent circuit for NiMn-4-700 and NiMn-10-700; TEM-EDS results for NiMn-4-700 and NiMn-10-700; discharge profiles of the first cycle at various rates for NiMn-4-700 and NiMn-10-700; GITT profiles for NiMn-4-700 and NiMn-10-700 (PDF)

■ AUTHOR INFORMATION

Corresponding Author

Shinichi Komaba – Department of Applied Chemistry, Tokyo University of Science, Shinjuku, Tokyo 162-8601, Japan; orcid.org/0000-0002-9757-5905; Email: komaba@rs.tus.ac.jp

Authors

Eun Jeong Kim – Department of Applied Chemistry, Tokyo University of Science, Shinjuku, Tokyo 162-8601, Japan

Ryoichi Tatara – Department of Applied Chemistry, Tokyo University of Science, Shinjuku, Tokyo 162-8601, Japan; orcid.org/0000-0002-8148-5294

Tomooki Hosaka – Department of Applied Chemistry, Tokyo University of Science, Shinjuku, Tokyo 162-8601, Japan; orcid.org/0000-0002-5922-8320

Kei Kubota – Battery Materials Analysis Group, Center for Green Research on Energy and Environmental Materials (GREEN), National Institute for Materials Science (NIMS), Tsukuba, Ibaraki 305-0044, Japan; orcid.org/0000-0001-8941-3650

Shinichi Kumakura – Umicore Japan KK, Minato, Tokyo 107-6026, Japan

Complete contact information is available at: <https://pubs.acs.org/doi/10.1021/acsaem.3c02462>

Notes

The authors declare no competing financial interest.

■ ACKNOWLEDGMENTS

E.J.K thanks Shun Nakajima for SEM measurements of $(\text{Ni}_{0.38}\text{Mn}_{0.62})\text{(OH)}_2$ precursors. This study was partially funded by the Ministry of Education, Culture, Sports, Science, and Technology (MEXT) Program: Data Creation and Utilization Type Materials Research and Development Project (JPMXP 1122712807), CREST (Grant No. JPMJCR21O6), and JSPS KAKENHI (Grant Nos. JP20H02849, JP21K14724, JP21K20561, JP22K14772, and JP23K13829). The authors are grateful to Dr. T. Ichihashi and Prof. Y. Idemoto of the Tokyo University of Science for TEM measurements. R.T. thanks the Takahashi Industrial and Economic Research Foundation and the ECSJ Kanto branch research grant.

■ REFERENCES

- (1) Komaba, S. Sodium-Driven Rechargeable Batteries: An Effort towards Future Energy Storage. *Chem. Lett.* **2020**, *49* (12), 1507–1516.
- (2) Kim, E. J.; Ramesh, K. P.; Gossage, Z. T.; Kubota, K.; Hosaka, T.; Royichi, T.; Komaba, S. Active Material and Interphase Structures Governing Performance in Sodium and Potassium Ion Batteries. *Chem. Sci.* **2022**, *13* (21), 6121–6158.
- (3) Yoda, Y.; Kubota, K.; Isozumi, H.; Horiba, T.; Komaba, S. Poly- γ -Glutamate Binder to Enhance Electrode Performances of P2-Na₂/3Ni₁/3Mn₂/3O₂ for Na-Ion Batteries. *ACS Appl. Mater. Interfaces* **2018**, *10* (13), 10986–10997.
- (4) Konarov, A.; Choi, J. U.; Bakenov, Z.; Myung, S. T. Revisit of Layered Sodium Manganese Oxides: Achievement of High Energy by Ni Incorporation. *J. Mater. Chem. A* **2018**, *6* (18), 8558–8567.
- (5) Risthaus, T.; Chen, L.; Wang, J.; Li, J.; Zhou, D.; Zhang, L.; Ning, D.; Cao, X.; Zhang, X.; Schumacher, G.; Winter, M.; Paillard, E.; Li, J. P3 Na 0.9 Ni 0.5 Mn 0.5 O 2 Cathode Material for Sodium Ion Batteries. *Chem. Mater.* **2019**, *31* (15), 5376–5383.
- (6) Wang, Q.; Mariyappan, S.; Vergnet, J.; Abakumov, A. M.; Rouse, G.; Rabuel, F.; Chakir, M.; Tarascon, J. M. Reaching the Energy Density Limit of Layered O₃-NaNi_{0.5}Mn_{0.5}O₂ Electrodes via Dual Cu and Ti Substitution. *Adv. Energy Mater.* **2019**, *9* (36), 1901785.
- (7) Somerville, J. W.; House, R. A.; Tapia-Ruiz, N.; Sobkowiak, A.; Ramos, S.; Chadwick, A. V.; Roberts, M. R.; Maitra, U.; Bruce, P. G. Identification and Characterisation of High Energy Density P2-Type Na₂/3[Ni₁/3-Y/2Mn₂/3-y/2Fe]O₂ compounds for Na-Ion Batteries. *J. Mater. Chem. A* **2018**, *6* (13), 5271–5275.
- (8) Kubota, K.; Fujitani, N.; Yoda, Y.; Kuroki, K.; Tokita, Y.; Komaba, S. Impact of Mg and Ti Doping in O₃ Type NaNi₁/2Mn₁/2O₂ on Reversibility and Phase Transition during Electrochemical Na Intercalation. *J. Mater. Chem. A* **2021**, *9* (21), 12830–12844.
- (9) Singh, G.; Tapia-Ruiz, N.; Lopez Del Amo, J. M.; Maitra, U.; Somerville, J. W.; Armstrong, A. R.; Martinez De Iarduya, J.; Rojo, T.; Bruce, P. G. High Voltage Mg-Doped Na_{0.67}Ni_{0.3}-XMgxMn_{0.7}O₂ (x = 0.05, 0.1) Na-Ion Cathodes with Enhanced Stability and Rate Capability. *Chem. Mater.* **2016**, *28* (14), 5087–5094.
- (10) Kubota, K.; Yoda, Y.; Komaba, S. Origin of Enhanced Capacity Retention of P2-Type Na₂/3 Ni₁/3-x Mn₂/3 Cu_x O₂ for Na-Ion Batteries. *J. Electrochem. Soc.* **2017**, *164* (12), A2368–A2373.
- (11) Yoshida, H.; Yabuuchi, N.; Kubota, K.; Ikeuchi, I.; Garsuch, A.; Schulz-Dobrick, M.; Komaba, S. P2-Type Na₂/3Ni₁/3Mn₂/3-xTi_xO₂ as a New Positive Electrode for Higher Energy Na-Ion Batteries. *Chem. Commun.* **2014**, *50* (28), 3677–3680.
- (12) Wang, P. F.; Yao, H. R.; Liu, X. Y.; Zhang, J. N.; Gu, L.; Yu, X. Q.; Yin, Y. X.; Guo, Y. G. Ti-Substituted NaNi_{0.5}Mn_{0.5}-XTi_xO₂ Cathodes with Reversible O₃-P3 Phase Transition for High-Performance Sodium-Ion Batteries. *Adv. Mater.* **2017**, *29* (19), 1700210.
- (13) Alvarado, J.; Ma, C.; Wang, S.; Nguyen, K.; Kodur, M.; Meng, Y. S. Improvement of the Cathode Electrolyte Interphase on P2-Na₂/3Ni₁/3Mn₂/3O₂ by Atomic Layer Deposition. *ACS Appl. Mater. Interfaces* **2017**, *9* (31), 26518–26530.
- (14) Hwang, J. Y.; Yu, T. Y.; Sun, Y. K. Simultaneous MgO Coating and Mg Doping of Na[Ni_{0.5}Mn_{0.5}]O₂ Cathode: Facile and Customizable Approach to High-Voltage Sodium-Ion Batteries. *J. Mater. Chem. A* **2018**, *6* (35), 16854–16862.
- (15) Ryu, H. H.; Han, G.; Yu, T. Y.; Sun, Y. K. Enhanced Cycling Stability of O₃-Type Na[Ni_{0.5}Mn_{0.5}]O₂ Cathode through Sn Addition for Sodium-Ion Batteries. *J. Phys. Chem. C* **2021**, *125* (12), 6593–6600.
- (16) Darga, J.; Manthiram, A. Facile Synthesis of O₃-Type NaNi_{0.5}Mn_{0.5}O₂ Single Crystals with Improved Performance in Sodium-Ion Batteries. *ACS Appl. Mater. Interfaces* **2022**, *14*, 52729–52737.
- (17) Langdon, J.; Manthiram, A. A Perspective on Single-Crystal Layered Oxide Cathodes for Lithium-Ion Batteries. *Energy Storage Mater.* **2021**, *37*, 143–160.
- (18) Han, G. M.; Kim, Y. S.; Ryu, H. H.; Sun, Y. K.; Yoon, C. S. Structural Stability of Single-Crystalline Ni-Rich Layered Cathode upon Delithiation. *ACS Energy Lett.* **2022**, *7* (9), 2919–2926.

- (19) Trevisanello, E.; Ruess, R.; Conforto, G.; Richter, F. H.; Janek, J. Polycrystalline and Single Crystalline NCM Cathode Materials—Quantifying Particle Cracking, Active Surface Area, and Lithium Diffusion. *Adv. Energy Mater.* **2021**, *11* (18), No. 2003400.
- (20) Ryu, H.-H.; Lee, S.; Yoon, C. S.; Sun, Y. Morphology-Dependent Battery Performance of Ni-Rich Layered Cathodes: Single-Crystal versus Refined Polycrystal. *ACS Energy Lett.* **2022**, *7*, 3072–3079.
- (21) Delmas, C.; Fouassier, C.; Hagemuller, P. Structural Classification And Properties Of The Layered Oxides. *Physica B+C* **1980**, *99*, 81–85.
- (22) Kim, E. J.; Maughan, P. A.; Bassey, E. N.; Clément, R. J.; Ma, L. A.; Duda, L. C.; Sehrawat, D.; Younesi, R.; Sharma, N.; Grey, C. P.; Armstrong, A. R. Importance of Superstructure in Stabilizing Oxygen Redox. *Adv. Energy Mater.* **2022**, *12*, No. 2102325.
- (23) Kim, E. J.; Ma, L. A.; Pickup, D. M.; Chadwick, A. V.; Younesi, R.; Maughan, P.; Irvine, J. T. S.; Armstrong, A. R. Vacancy-Enhanced Oxygen Redox Reversibility in P3-Type Magnesium-Doped Sodium Manganese Oxide Na_{0.67}Mg_{0.2}Mn_{0.8}O₂. *ACS Appl. Energy Mater.* **2020**, *3* (11), 10423–10434.
- (24) Linnell, S. F.; Hirsbrunner, M.; Imada, S.; Cibin, G.; Naden, A. B.; Chadwick, A. V.; Irvine, J. T. S.; Duda, L. C.; Armstrong, A. R. Enhanced Cycling Stability in the Anion Redox Material P3-Type Zn-Substituted Sodium Manganese Oxide. *ChemElectroChem* **2022**, *9* (11), 220240.
- (25) Linnell, S. F.; Kim, E. J.; Ma, L. A.; Naden, A.; Irvine, J.; Younesi, R.; Duda, L.; Armstrong, A. R. Effect of Ti Substitution on the Properties of P3 Structure Na₂/3Mn_{0.8}Li_{0.2}O₂ Showing a Ribbon Superlattice. *ChemElectroChem* **2022**, *9*, No. 2200929, DOI: 10.1002/celec.202200929.
- (26) Armstrong, A. R.; Paterson, A. J.; Robertson, A. D.; Bruce, P. G. Nonstoichiometric Layered Li_xMn_yO₂ with a High Capacity for Lithium Intercalation/Deintercalation. *Chem. Mater.* **2002**, *14* (2), 710–719.
- (27) Robertson, A. D.; Armstrong, A. R.; Paterson, A. J.; Duncan, M. J.; Bruce, P. G. Nonstoichiometric Layered Li_xMn_yO₂ Intercalation Electrodes - A Multiple Dopant Strategy. *J. Mater. Chem.* **2003**, *13* (9), 2367–2373.
- (28) Robertson, A. D.; Armstrong, A. R.; Bruce, P. G. Layered Li_xMn_{1-y}Co_yO₂ Intercalation Electrodes - Influence of Ion Exchange on Capacity and Structure upon Cycling. *Chem. Mater.* **2001**, *13* (7), 2380–2386.
- (29) Toby, B. H.; Von Dreele, R. B. GSAS-II: The Genesis of a Modern Open-Source All Purpose Crystallography Software Package. *J. Appl. Crystallogr.* **2013**, *46* (2), 544–549.
- (30) Yabuuchi, N.; Kubota, K.; Aoki, Y.; Komaba, S. Understanding Particle-Size-Dependent Electrochemical Properties of Li₂MnO₃-Based Positive Electrode Materials for Rechargeable Lithium Batteries. *J. Phys. Chem. C* **2016**, *120* (2), 875–885.
- (31) Zheng, J.; Yan, P.; Estevez, L.; Wang, C.; Zhang, J. G. Effect of Calcination Temperature on the Electrochemical Properties of Nickel-Rich LiNi_{0.76}Mn_{0.14}Co_{0.10}O₂ Cathodes for Lithium-Ion Batteries Jianming. *Nano Energy* **2018**, *49*, 538–548.
- (32) Kubota, K.; Komaba, S. Review-Practical Issues and Future Perspective for Na-Ion Batteries. *J. Electrochem. Soc.* **2015**, *162* (14), A2538–A2550.
- (33) Monyoncho, E.; Bissessur, R. Unique Properties of α -NaFeO₂: De-Intercalation of Sodium via Hydrolysis and the Intercalation of Guest Molecules into the Extract Solution. *Mater. Res. Bull.* **2013**, *48* (7), 2678–2686.
- (34) Kubota, K.; Kumakura, S.; Yoda, Y.; Kuroki, K.; Komaba, S. Electrochemistry and Solid-State Chemistry of NaMeO₂ (Me = 3d Transition Metals). *Adv. Energy Mater.* **2018**, *8* (17), 1703415.
- (35) Zheng, L.; Li, L.; Shunmugasundaram, R.; Obrovac, M. N. Effect of Controlled-Atmosphere Storage and Ethanol Rinsing on NaNi_{0.5}Mn_{0.5}O₂ for Sodium-Ion Batteries. *ACS Appl. Mater. Interfaces* **2018**, *10* (44), 38246–38254.
- (36) Sambandam, B.; Alfaruqi, M. H.; Park, S.; Lee, S.; Kim, S.; Lee, J.; Mathew, V.; Hwang, J. Y.; Kim, J. Validating the Structural (In)Stability of P3- And P2-Na_{0.67}Mg_{0.1}Mn_{0.9}O₂-Layered Cathodes for Sodium-Ion Batteries: A Time-Decisive Approach. *ACS Appl. Mater. Interfaces* **2021**, *13* (45), 53877–53891.
- (37) Parant, J. P.; Olazcuaga, R.; Devalette, M.; Fouassier, C.; Hagemuller, P. Sur Quelques Nouvelles Phases de Formule Na_xMnO₂ ($x \leq 1$). *J. Solid State Chem.* **1971**, *3* (1), 1–11.
- (38) Paulsen, J. M.; Dahn, J. R. Studies of the Layered Manganese Bronzes, Na [Mn_{1-x}M_x]O₂ with M = Co, Ni, Li, and [Mn_{1-x}M_x]O₂ Prepared by Ion-Exchange. *Solid State Ionics* **1999**, *126*, 3–24.
- (39) Braconnier, J. J.; Delmas, C.; Hagemuller, P. Etude Par Desintercalation Electrochimique Des Systemes Na_xCrO₂ et Na_xNiO₂. *Mater. Res. Bull.* **1982**, *17* (8), 993–1000.
- (40) Lu, Z.; Dahn, J. R. In Situ X-Ray Diffraction Study of P2-Na[Sub 2/3][Ni[Sub 1/3]Mn[Sub 2/3]]O[Sub 2]. *J. Electrochem. Soc.* **2001**, *148* (11), A1225.
- (41) Mendiboure, A.; Delmas, C.; Hagemuller, P. Electrochemical Intercalation and Deintercalation of Na_xMnO₂ Bronzes. *J. Solid State Chem.* **1985**, *57*, 323–331.
- (42) Pang, W. K.; Kalluri, S.; Peterson, V. K.; Sharma, N.; Kimpton, J.; Johannessen, B.; Liu, H. K.; Dou, S. X.; Guo, Z. Interplay between Electrochemistry and Phase Evolution of the P2-Type Na_x(Fe_{1/2}Mn_{1/2})O₂ Cathode for Use in Sodium-Ion Batteries. *Chem. Mater.* **2015**, *27* (8), 3150–3158.
- (43) Pfeiffer, L. F.; Li, Y.; Mundszinger, M.; Geisler, J.; Pfeifer, C.; Mikhailova, D.; Omar, A.; Baran, V.; Biskupek, J.; Kaiser, U.; Adelhelm, P.; Wohlfahrt-mehrens, M.; Passerini, S.; Axmann, P. Origin of Aging of a P2-Na_xMn_{3/4}Ni_{1/4}O₂ Cathode Active Material for Sodium-Ion Batteries. *Chem. Mater.* **2023**, *35* (19), 8065–8080.
- (44) Thackeray, M. M. Manganese Oxides for Lithium Batteries. *Prog. Solid State Chem.* **1997**, *25* (1–2), 1–71.
- (45) Chagas, L. G.; Buchholz, D.; Wu, L.; Vortmann, B.; Passerini, S. Unexpected Performance of Layered Sodium-Ion Cathode Material in Ionic Liquid-Based Electrolyte. *J. Power Sources* **2014**, *247*, 377–383.
- (46) Villars, P.; Hulliger, F. NiO RT Conductivity/Resistivity: Datasheet from “PAULING FILE Multinaries Edition” 2022 <https://materials.springer.com/isp/physical-property/docs/ppp-f73df1ee2594a3e0e4ed3ab01a421a64>.
- (47) Clément, R. J.; Lun, Z.; Ceder, G. Cation-Disordered Rocksalt Transition Metal Oxides and Oxyfluorides for High Energy Lithium-Ion Cathodes. *Energy Environ. Sci.* **2020**, *13* (2), 345–373.
- (48) Kim, H.; Kong, Y.; Seong, W. M.; Manthiram, A. Controlling the Microstructure of Cobalt-Free, High-Nickel Cathode Materials with Dopant Solubility for Lithium-Ion Batteries. *ACS Appl. Mater. Interfaces* **2023**, *15* (22), 26585–26592.
- (49) Kubota, K.; Miyazaki, M.; Kim, E. J.; Yoshida, H.; Barpanda, P.; Komaba, S. Structural Change Induced by Electrochemical Sodium Extraction from Layered O₃-NaMnO₂. *J. Mater. Chem. A* **2021**, *9*, 26810–26819.
- (50) Kubota, K.; Ikeuchi, I.; Nakayama, T.; Takei, C.; Yabuuchi, N.; Shiiba, H.; Nakayama, M.; Komaba, S. New Insight into Structural Evolution in Layered NaCrO₂ during Electrochemical Sodium Extraction. *J. Phys. Chem. C* **2015**, *119* (1), 166–175.
- (51) Yu, T. Y.; Ryu, H. H.; Han, G.; Sun, Y. K. Understanding the Capacity Fading Mechanisms of O₃-Type Na[Ni_{0.5}Mn_{0.5}]O₂ Cathode for Sodium-Ion Batteries. *Adv. Energy Mater.* **2020**, *10* (37), 2001609.
- (52) Jung, R.; Metzger, M.; Maglia, F.; Stinner, C.; Gasteiger, H. A. Chemical versus Electrochemical Electrolyte Oxidation on NMC111, NMC622, NMC811, LNMO, and Conductive Carbon. *J. Phys. Chem. Lett.* **2017**, *8* (19), 4820–4825.
- (53) Jung, R.; Metzger, M.; Maglia, F.; Stinner, C.; Gasteiger, H. A. Oxygen Release and Its Effect on the Cycling Stability of LiNi_xMn_yCo_zO₂ (NMC) Cathode Materials for Li-Ion Batteries. *J. Electrochem. Soc.* **2017**, *164* (7), A1361–A1377.
- (54) House, R. A.; Maitra, U.; Jin, L.; Lozano, J. G.; Somerville, J. W.; Rees, N. H.; Naylor, A. J.; Duda, L. C.; Massel, F.; Chadwick, A. V.; Ramos, S.; Pickup, D. M.; McNally, D. E.; Lu, X.; Schmitt, T.; Roberts, M. R.; Bruce, P. G. What Triggers Oxygen Loss in Oxygen Redox Cathode Materials? *Chem. Mater.* **2019**, *31* (9), 3293–3300.

(55) Oswald, S.; Bock, M.; Gasteiger, H. A. Elucidating the Implications of Morphology on Fundamental Characteristics of Nickel-Rich NCMs: Cracking, Gassing, Rate Capability, and Thermal Stability of Poly- and Single-Crystalline NCM622. *J. Electrochem. Soc.* **2022**, *169* (5), No. 050501.

(56) Sathiya, M.; Thomas, J.; Batuk, D.; Pimenta, V.; Gopalan, R.; Tarascon, J. M. Dual Stabilization and Sacrificial Effect of Na₂CO₃ for Increasing Capacities of Na-Ion Cells Based on P2-NaxMO₂ Electrodes. *Chem. Mater.* **2017**, *29* (14), 5948–5956.

(57) Shen, Z.; Cao, L.; Rahn, C. D.; Wang, C.-Y. Least Squares Galvanostatic Intermittent Titration Technique (LS-GITT) for Accurate Solid Phase Diffusivity Measurement. *J. Electrochem. Soc.* **2013**, *160* (10), A1842–A1846.

(58) Hosaka, T.; Fukabori, T.; Kojima, H.; Kubota, K.; Komaba, S. Effect of Particle Size and Anion Vacancy on Electrochemical Potassium Ion Insertion into Potassium Manganese Hexacyanoferrates. *ChemSusChem* **2021**, *14* (4), 1166–1175.